

Experimental Study of Underwater Acoustic Reconfigurable Intelligent Surfaces with In-Phase and Quadrature Modulation

Yu Luo*, Lina Pu†, Aijun Song‡

*ECE Department, Mississippi State University, Mississippi State, MS, 39759, USA

†Department of Computer Science, University of Alabama, Tuscaloosa, AL 35487, USA

‡Department of Electrical and Computer Engineering, University of Alabama, Tuscaloosa, AL 35487, USA

Email: yu.luo@ece.msstate.edu, lina.pu@ua.edu, song@eng.ua.edu

Abstract— This paper presents an underwater acoustic reconfigurable intelligent surfaces (UA-RIS) designed for long-range, high-speed, and environmentally friendly communication in oceanic environments. The proposed UA-RIS comprises multiple pairs of acoustic reflectors that utilize in-phase and quadrature (IQ) modulation to flexibly control the amplitude and phase of reflected waves. This capability enables precise beam steering to enhance or attenuate sound levels in specific directions. A prototype UA-RIS with 4×6 acoustic reflection units is constructed and tested in both tank and lake environments to evaluate performance. The experimental results indicate that the prototype is capable of effectively pointing reflected waves to targeted directions while minimizing side lobes using passive IQ modulation. Field tests reveal that deploying the UA-RIS on the sender side considerably extends communication ranges by 28% in deep water and 46% in shallow waters. Furthermore, with a fixed communication distance, positioning the UA-RIS at the transmitter side substantially boosts data rates, with an average increase of 63.8% and peaks up to 96%. When positioned on the receiver side, the UA-RIS can expand the communication range in shallow and deep water environments by 40.6% and 66%, respectively. Moreover, placing the UA-RIS close to the receiver enhances data rates by an average of 80.3%, reaching up to 163% under certain circumstances.

Index Terms—Reconfigurable intelligent surface (RIS), underwater acoustic communication, in-phase and quadrature (IQ) modulation, lake tests.

I. INTRODUCTION

In recent years, radio frequency reconfigurable intelligent surfaces (RF-RIS) have emerged as a promising technology to enhance communication quality for 5G and beyond networks [1]. By dynamically adjusting the amplitude and phase of reflected electromagnetic waves with the load network, RIS can precisely steer beams in specific directions. This capability enhances signal strength at the receiver while reducing interference in surrounding environments, thereby improving the overall performance of wireless communication networks [2].

Although extensive research has been conducted for RIS in radio environments, bringing this cutting-edge technology into underwater environments remains a complex problem. In water, the transmission range of electromagnetic (EM) waves is severely restricted due to significant absorption attenuation. Currently, acoustic communication is still the principal method for mid-range and long-range communication in marine settings. However, the physical properties of acoustic waves are completely distinct from those of radio signals, rendering existing RF-RIS unsuitable for direct application in water. At present, only limited studies explore the design of underwater acoustic RIS (UA-RIS) [3], [4].

Our work demonstrates that UA-RIS can significantly extend communication range, enhance data rates, and opti-

mize channel utilization for underwater acoustic networks. Nevertheless, to transition UA-RIS from theory to practical application, we must overcome a series of distinct challenges:

- a) **Constrained energy supply:** UA-RIS systems operate in maritime settings, where stable power infrastructure is often absent. Consequently, UA-RIS units, especially those situated on the ocean floor, require energy harvesting from sources such as ocean waves or microorganisms for self-sufficiency [5]. Nonetheless, the power density provided by these sustainable sources tends to be low, presenting substantial challenges for UA-RIS design. Addressing this limitation necessitates meticulous planning in both system design and power management strategy.
- b) **High dynamic range of acoustic signal:** To mitigate the high propagation attenuation over long range, acoustic modems are designed with high source levels. As a result, the intensity of sound waves reaching the UA-RIS varies widely with the distance. This high dynamic strength of incident waves poses a substantial challenge for system development. The reflection unit must be able to handle both weak and strong signals, requiring versatile load network configurations to accurately reflect waves with the intended amplitude and phase.
- c) **Low acoustic frequency:** The frequency employed for mid-range and long-range acoustic communication is significantly lower than that of RF systems due to the substantial frequency-dependent absorption of acoustic waves in water. Consequently, the wavelength of acoustic signals becomes long. In this context, the phase of the reflected waves cannot be adjusted by changing the length of the transmission line, a method commonly applied in RF-RIS. UA-RIS necessitates more efficient phase-shift mechanisms to effectively control wave reflection.

To address the above issues, we proposed a UA-RIS, which can automatically pair acoustic reflectors based on the angles of reflected waves. Each pair of reflectors then performs in-phase and quadrature (IQ) modulation to direct the reflected beam in specific directions. Compared to the 1-bit and 2-bit coding schemes widely used in RF-RIS for beam steering [1], [6], the IQ modulation offers significantly enhanced flexibility. Specifically, traditional multi-bit coding schemes can produce only a finite number of phase states. This limitation results in coarse control over the reflected waves, leading to less precise beam direction. Furthermore, multi-bit coding schemes typically do not allow altering the amplitude of the reflected wave, resulting in higher side lobes in the beam pattern, which can cause unexpected interference issues. In contrast, IQ

modulation enables the formation of reflected waves with arbitrary amplitude and phase, supporting more sophisticated array processing methods such as minimum variance distortionless response (MVDR) and linearly constrained minimum variance (LCMV) [7]. As a result, the reflected waves can be accurately directed in the desired directions without introducing strong interferences in environments.

A prototype equipped with 24 (6×4) acoustic reflectors is implemented to assess the effectiveness of the proposed UA-RIS. Each reflector is constructed with a Tonpitz structure to reflect incident waves efficiently at 28 kHz frequency. The complete assembly, which includes the matching circuit and the load network, is controlled by an ultra-low-power microcontroller (MCU) and multiple I/O expanders. The whole system has been carefully optimized to reliably manage high-dynamic acoustic signals originating from various acoustic facilities and mobile platforms.

We carried out comprehensive experiments in tank and lake environments to evaluate the performance of the proposed work across various configurations. The experimental results show that the UA-RIS can flexibly enhance or attenuate the strength of acoustic waves in specific directions. By deploying the UA-RIS with 24 reflection units at the sender side, the data rate of acoustic communication can be improved by an average of 63.8% (up to 96%), or the communication range can be extended by 28% and 46% in deep water and shadow water environments, respectively. When positioned near the receiver, the UA-RIS extends the communication range in shallow and deep water environments by 40.6% and 66%, respectively. Additionally, situating the UA-RIS adjacent to the receiver boosts data rates by an average of 80.3%, with increases up to 163% under certain conditions.

To summarize, our work makes three key contributions:

- a) We thoroughly investigate the implementation challenges of using RIS technology to achieve long-range, high-speed, and environmentally friendly underwater acoustic communications.
- b) An IQ modulation scheme is developed for UA-RIS that allows to generation of reflected signals with arbitrary amplitude and phase shifts. This technique ensures precise steering of the reflected waves, directing them effectively while minimizing interference in unintended directions.
- c) Both tank and lake experiments are conducted to validate the feasibility of the UA-RIS. The results confirm that our system can significantly enhance the quality of receiving signals in underwater environments for long-range and high-speed acoustic communications.

The structure of this paper is as follows: Section II reviews related work on UA-RIS. Section III explores two applications to motivate our work. Section IV examines the benefits of using IQ modulation in UA-RIS. Section V provides a detailed description of the UA-RIS hardware design. Lastly, Section VI presents an experimental validation of the system performance.

II. RELATED WORK

A. RIS in Terrestrial Radio Environments

The advent of RF-RIS technology lies in the study of metamaterials, which are composed of periodic structures with scales that are smaller than the wavelength of interacting electromagnetic (EM) waves. These metamaterials can resonate

with incident EM fields, consequently producing a specific EM response on the surface with a precise design of the surface architecture [8], [9].

Metasurfaces have the potential to minimize radar cross-sections (RCSs), thereby improving the stealthiness of aircraft and target objects. As studied in [10], each unit on the metasurface can be configured to reflect incident EM waves in one of two states: in-phase or out-of-phase. By combining these states across the surface with different patterns, it is possible to minimize the intensity of the backscattered signal.

Over the past decade, metasurfaces have experienced significant evolution, especially in their enhanced ability to manipulate the phase and amplitude of incident waves. Such advancements have led to the development of RIS, capable of forming arbitrary reflected beams in space. This innovation plays a pivotal role in improving communication quality and is regarded as a promising technology for the next generation of wireless networks [11], [12].

As introduced in [13], the phase response of a RIS can be electronically controlled by adding a varactor diode at the radiating edge of a patch antenna. This technique enables each RIS unit to achieve a tunable phase range of up to 180° . Expanding upon this idea, [14] introduces a modification where microstrip patches are loaded with varactor diodes to enable broader beam forming. Such a modification changes the resonant frequency of each reflector unit, thereby affecting the phase of the scattered signal. The RIS units developed in their work exhibited more than 320° of phase agility at 5.5 GHz, while sustaining a reflection efficiency above 70%. The architecture of the RIS presented in [14] has been applied in [15] to enhance spectrum sharing at the 2.4 GHz frequency. This enhancement is realized by improving the link quality between communicating parties while canceling out interference to other network participants through the RF-RIS.

The method involving the varactor to enable arbitrary phase shifts for extensive beamforming is further explored in [16]. Their study demonstrates that adjusting the varactor's bias voltage between 0 V to 19 V can produce a phase shift range from approximately -110° to 110° at 5.8 GHz, while maintaining reflection efficiency above 70%. In an indoor setting, the implemented RIS can overcome a 30 cm thick concrete barrier and achieve a 26 dB gain at the receiver. For outdoor applications, the system delivered a 14 dB gain, facilitating high-speed communications across a distance of 500 meters.

In [17], a practical phase shift model is proposed for RIS. Diverging from traditional models that typically assume the RIS can alter the phase of reflected waves between $-\pi$ and π , while maintaining a constant amplitude of 1, the new model takes into account the coupling between the amplitude and the phase shift of reflected waves, aligning with the experimental results presented in [18]. This refined model is advantageous for designing optimal reflection coefficients for RIS, as it can balance between the amplitude and the phase of signals reflected by each unit. This ensures that the aggregate of the signals reflected towards the receiver has the maximum SNR.

B. RIS in Underwater Acoustic Environments

Inspired by achievements of metasurface in radio applications, the underwater acoustics sector is progressively embracing this new technology for its ability to manipulate the pattern of reflected waves. These artificial structures demonstrate

proficiency in minimizing the scattering cross-section (SCS) of sonar systems. Such an advancement is of strategic importance, especially for enhancing stealth properties in military applications.

An example of the above application is the 2-bit coding metasurface developed in [19]. This metasurface features four distinct types of elements. Each element is a steel plate punctured with four square holes at different depths, specifically engineered to shift the phase of reflected waves by 0 , $\pi/2$, π , and $3\pi/2$. Through a meticulous arrangement of these elements, the design successfully attenuates the intensity of backscattered waves by at least 10 dB, proving particularly effective within the 14.3 kHz to 40.5 kHz frequency range.

Beyond metamaterials, conventional piezoelectric ceramics can also electronically manipulate the phase and amplitude of reflected waves. For instance, the research conducted in [20] showcases the development of an underwater backscatter array designed for long-distance passive acoustic communication. Utilizing the Van Atta array architecture, this system enables the reflected acoustic waves to automatically align with the direction of the incoming waves, eliminating the need for active components within the circuit. According to experimental data, the Van Atta backscatter array is capable of achieving a round-trip communication range exceeding 300 meters with a bit error rate (BER) of 10^{-3} .

The design of a UA-RIS for high-data-rate and long-range communication is explored in [3]. Each unit of the proposed UA-RIS comprises a piezoelectric coil sandwiched between two metal plates to reflect acoustic waves. The resonant impedance of the piezoelectric reflector is adjusted using a varactor and an MCU, allowing for continuous tuning of the acoustic unit's elasticity. This adjustment introduces additional phase shifts in reflected waves.

The study in [4] investigates wide-band beamforming using the UA-RIS architecture developed in [3]. This approach aims to neutralize two types of dispersion effects: element dispersion within each piezoelectric reflector and array dispersion across the acoustic RIS. By doing so, the directivity of the reflected waves becomes frequency-independent, allowing wideband signals to achieve consistent beamforming results across various frequency components. The effectiveness of the proposed architecture is assessed using COMSOL and the Bellhop simulator.

III. APPLICATIONS OF UA-RIS

In this section, we introduce two potential applications of using UA-RIS for achieving ultra-long-distance and environmentally friendly underwater acoustic communications.

A. Environmentally Friendly Acoustic Communication

In oceans, underwater wildlife, such as dolphins and whales, depend critically on acoustic signals for communication, hunting, and navigation [21]. As shown in Fig. 1, bottlenose dolphins use frequencies from 200 Hz to 24 kHz for whistles and 200 Hz to 150 kHz for echolocation clicks, while killer whales' echolocation typically occurs within the 12 kHz to 25 kHz range [22]. These frequencies coincide with those used by human-made acoustic devices, potentially leading to disruptions or even damage to the auditory systems of marine life. Consequently, ensuring the coexistence of marine wildlife

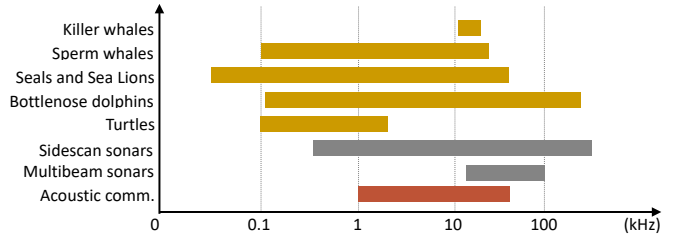


Figure 1: Typical channel usage of marine life and human-made acoustic systems.

is an essential factor in designing next-generation underwater communication systems.

The UA-RIS technology offers a viable solution to achieve the aforementioned goal. With the assistance of RIS, acoustic modems can transmit data at a lower sound level, reducing their environmental footprint, and thereby minimizing the interference of sound devices with the acoustic channel. Furthermore, UA-RIS directs the reflected signal towards a specific direction rather than dispersing them throughout the space. This approach not only diminishes interference but also improves channel utilization in the spatial domain.

B. Long-Range Underwater Communication

For long-range communication, traditional underwater acoustic systems usually operate at low frequencies to mitigate propagation attenuation. This approach often requires either larger acoustic transducers or increased transmission power, which in turn shortens battery life. In contrast, UA-RIS provides an alternative by allowing the use of compact, low-power transducers for effective long-range communication effectively.

To achieve the above objective, multiple UA-RIS units are strategically deployed at both the ocean's surface and its depths. As illustrated in Fig. 2, the surface UA-RIS unit is solar-powered and mounted on a buoy, while the deep-sea UA-RIS is connected to a wirewalker [23], a fully passive device that harvests energy from the motion of ocean waves.

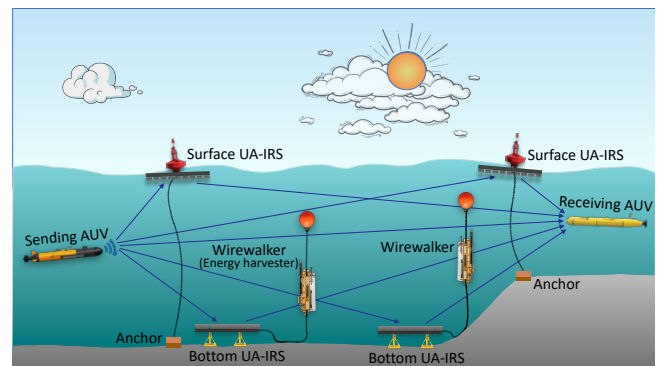


Figure 2: UA-RIS assisted long-range underwater acoustic communication network.

By meticulously designing the system, UA-RIS units precisely direct the source signal toward the intended receiver during transmission. This approach coherently combines multiple acoustic waves reflected by the UA-RIS units at the receiver side, thereby substantially boosting the signal-to-noise

ratio (SNR). As a result, it facilitates extended communication ranges, even at higher frequencies, by effectively preserving signal strength over long distances.

IV. IQ MODULATION FOR UA-RIS

This section explores the IQ modulation technique utilized in our UA-RIS. We begin by examining the challenge of implementing arbitrary phase shifts within UA-RIS, followed by a description of how IQ modulation addresses this issue. Subsequently, we discuss the benefits of IQ modulation, highlighting its feasibility, flexibility, and interference reduction.

A. Challenges of Implementing Arbitrary Phase-Shift in UA-RIS

In an ideal RIS, each reflecting unit should independently and passively control both the amplitude and phase of reflected waves. However, implementing this functionality presents challenges in practical systems due to hardware constraints. As a result, most existing RF-RIS designs maintain a fixed amplitude and focus on modifying the phase of the reflected wave. This is typically achieved by adjusting the load impedance of each reflection unit using varactor diodes [16], [17]. Unfortunately, this approach is not viable for UA-RIS due to the low frequency of acoustic signal, as will be analyzed next.

When a wave propagates through mediums with discontinuous impedances, reflection occurs. The reflection coefficient, denoted by Γ , is calculated using:

$$\Gamma = \frac{Z_L - Z_0}{Z_L + Z_0}, \quad (1)$$

where Z_L represents the load impedance, and Z_0 is the characteristic impedance of the transmission line.

According to equation (1), an RIS with a characteristic impedance of 50Ω , typical for RF transmission lines, requires load impedances of $-121j\Omega$ and $-50j\Omega$ to generate reflected waves with the same amplitude as the incident wave but with phase shifts of -45° and -90° , respectively. Assuming a signal frequency of 30 GHz is selected for mmWave communication, these load impedances correspond to capacitances of approximately 44 pF and 106 pF, respectively. Commercial varactor diodes, such as the ZC836A [24] and NTE618 [25], can continuously vary capacitance within this range by adjusting the reverse bias voltage applied to their p-n junctions, thereby enabling arbitrary phase shifts of the reflected waves.

However, the frequencies used for middle-range or long-range acoustic communications are typically low, often below 50 kHz. Under these conditions, the capacitance of the varactor diode needs to change significantly to shift the phase of reflected waves. For example, maintaining the conditions from the previous analysis but reducing the signal frequency to 50 kHz, the load network in the RIS would need to adjust the capacitance from 26 nF to 64 nF to shift the phase of the incident wave from -45° to -90° . This range exceeds the capabilities of most commercial varactor diodes. Consequently, a new method is essential to implement arbitrary phase shifts for UA-RIS.

B. Implementation of IQ modulation

In the proposed UA-RIS, we employ IQ modulation to generate reflected waves with arbitrary amplitude and phase

shift. To implement this scheme, the MCU automatically pairs acoustic reflectors according to the angles of reflected waves. Subsequently, one reflector in each pair produces an in-phase or antiphase component, shifting the phase of the reflected waves by 0° or 180° . The other reflector generates a quadrature component, shifting the phase of the reflected waves by 90° relative to the incident signal. By precisely controlling the amplitude of the in-phase, antiphase, and quadrature components, the UA-RIS can synthesize reflected waves with any desired phase in space, as dictated by trigonometric identities:

$$\begin{aligned} \sin(\omega t + \phi) &= \sin \phi \cos \omega t + \cos \phi \sin \omega t \\ &\triangleq A_I \cos \omega t + A_Q \sin \omega t, \end{aligned} \quad (2)$$

where ω is angular frequency; t is time; ϕ is arbitrary phase shift between $-\frac{\pi}{2}$ and $\frac{\pi}{2}$; A_I is the amplitude of in-phase ($A_I \geq 0$) or antiphase component ($A_I < 0$); A_Q is the amplitude of the quadrature component.

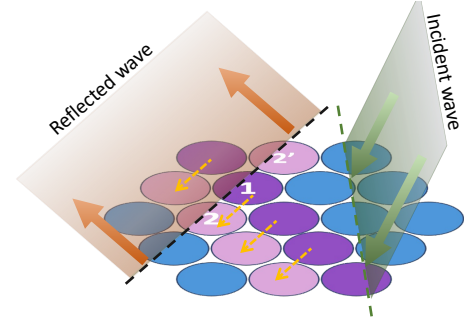


Figure 3: IQ modulation for arbitrary phase shift.

Fig. 3 illustrates how IQ modulation operates. In the diagram, each circle represents an acoustic reflector, the size of which is one wavelength to efficiently reflect the incident waves. In the figure, the green plane indicates the direction of the incident wave, while the orange plane designates the target direction for the reflected waves.

To execute IQ modulation, only reflectors located on the wavefront of the reflected wave (as marked by the black dotted line in the figure) can be paired. For example, reflector 1 can be paired with reflector 2 or 2'. With this configuration, the projection positions of the paired reflectors along the direction of the reflected waves align. Consequently, positional differences between paired reflectors do not result in additional phase shifts in the direction of the reflected wave. This setup enables the paired reflectors to function collectively as a single reflector, facilitating precise beam steering.

It is important to recognize that the phase of the incident wave received by each reflector in a pair may differ. This discrepancy arises because the projection positions of the paired reflectors along the wavefront of the incident signals do not always align, as depicted in Fig. 3, where the green dotted line (representing the wavefront of the incident wave) is not parallel to the black dotted line. Therefore, the UA-RIS must correct these phase differences to ensure that the reflected waves generated by the pair of reflectors remain orthogonal, which is crucial for effective IQ modulation.

To address the aforementioned issue, the UA-RIS must tailor the reflection coefficients of each reflector based on the angle of the incident wave. Taking the pair of reflectors 1 and 2 in Fig. 3 as an example, assume the incident waves received by

reflector 1 and reflector 2 are $\cos(\omega t + \phi_1)$ and $\cos(\omega t + \phi_2)$, respectively. The MCU then adjusts the impedance of the load network to set the reflection coefficient of reflectors 1 and 2 to A_1 and jA_2 , respectively, where j represents the imaginary component with 90° phase shift. This configuration results in the sum of the acoustic waves reflected by reflectors 1 and 2 being:

$$\begin{aligned} & A_1 \cos(\omega t + \phi_1) + A_2 \cos\left(\omega t + \frac{\pi}{2} + \phi_2\right) \\ = & (A_1 \cos \phi_1 + A_2 \sin \phi_2) \cos \omega t \\ & + (A_1 \sin \phi_1 + A_2 \cos \phi_2) \sin \omega t. \end{aligned} \quad (3)$$

Comparing (3) with (2) reveals that $(A_1 \cos \phi_1 + A_2 \sin \phi_2)$ is the amplitude of the in-phase or antiphase component, while $(A_1 \sin \phi_1 + A_2 \cos \phi_2)$ is the amplitude of the quadrature components for IQ modulation.

To direct the reflected signal towards the desired direction, assume that the waveform synthesized by reflectors 1 and 2 is represented as:

$$\cos(\omega t + \phi_r) = \cos \phi_r \cos \omega t + \sin \phi_r \sin \omega t, \quad (4)$$

where $\phi_r \in [-\frac{\pi}{2}, \frac{\pi}{2}]$. Then, by combining (3) and (4), the coefficients A_1 and A_2 of the reflectors 1 and 2 can be derived as follows:

$$A_1 = \begin{vmatrix} \cos \phi_r & \sin \phi_2 \\ \sin \phi_r & \cos \phi_2 \end{vmatrix} \quad \text{and} \quad A_2 = \begin{vmatrix} \cos \phi_1 & \cos \phi_r \\ \sin \phi_1 & \sin \phi_r \end{vmatrix}, \quad (5)$$

where $|\mathbf{A}|$ indicates the determinant of a matrix \mathbf{A} . Using (5), the MCU can calculate the reflection coefficient for each reflector based on the angles of the incident and reflected waves. This enables the synthesis of reflected waves with arbitrary phases, facilitating precise beam steering as required.

V. HARDWARE ARCHITECTURE

This section outlines the hardware design of UA-RIS, beginning with an introduction to the structure of the acoustic reflector and the circuitry designed for efficient IQ modulation. Following this, we will discuss several critical considerations essential for real-world implementation.

A. Structure and Circuit of Acoustic Reflector

1) *Reflector Structure:* Our work concentrates on acoustic signals within the mid-frequency range between 10 kHz and 50 kHz. As a result, the Tonpiliz structure is selected for constructing the reflection unit, due to its superior electroacoustic conversion efficiency and effective impedance matching between the piezoelectric materials and water. This configuration allows for the flexible adjustment of the amplitude and phase of reflected waves.

Fig. 4 depicts the structure of the reflector used in our UA-RIS, consisting of a head mass, two PZT disks equipped with electrodes, a prestressing rod, and a tail mass. The head mass, a round cone cast from aluminum alloy, ensures effective oscillation along the central axis without placing undue stress on any component of the reflector. Situated behind the head mass are two PZT disks, strung together with a prestressing

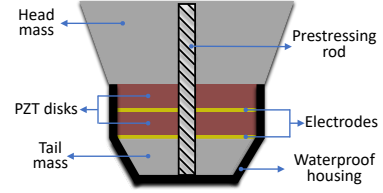


Figure 4: Tonpiliz reflector used in our UA-RIS.

rod and separated by copper sheets that link to the subsequent circuit to regulate the reflector's load impedance. The tail mass at the rear reflects backward-traveling vibrations, ensuring that the acoustic wave is projected forward.

In practical applications, achieving sufficient directional gain for a high-performance UA-RIS typically necessitates a substantial array of acoustic reflectors, impacting the size and cost of the system. Consequently, our UA-RIS is equipped with only two PZT plates per reflector, each with 38 mm in diameter and 5 mm in height. This build significantly reduces size, weight, and cost, facilitating widespread deployment of UA-RIS in marine environments.

2) *Circuit Design:* Fig. 5 presents the circuit architecture of the proposed UA-RIS, consisting three primary components: a matching network, a load network, and a control & processing unit. Next, we will delve into a detailed explanation of each component.

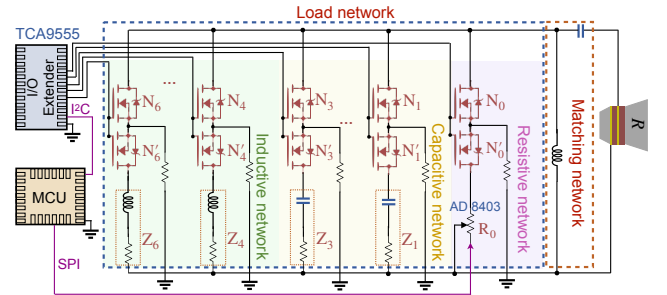


Figure 5: Architecture of the UA-RIS.

In the circuit, the matching network aligns the impedance of all reflectors to a real number, which is represented as Z_0 in (1). Subsequently, the reflection coefficient for each reflector is modulated by linking different stages of the load network to the matching circuit. The connection of each stage is controlled through a pair of n-type metal-oxide-semiconductor (NMOS) transistors, whose ON/OFF states are regulated by TCA9555 I/O extenders and an ATmega256RFR2 MCU.

The load network comprises three subnetworks: a resistor network, a capacitive network, and an inductive network. The resistor network has only one stage designed to generate the in-phase or antiphase component required for IQ modulation. Conversely, both the capacitive and inductive networks feature three stages each, dedicated to producing the quadrature component for IQ modulation.

Resistor network contains an AD8403AR50 programmable potentiometer, whose resistance is managed by the MCU via the serial peripheral interface (SPI) protocol. Let R_0 represent the resistance of this potentiometer. According to the reflection coefficient presented in (1), when the load connected to the matching circuit is non-reactive and Z_0 is a real number, Γ has

no imaginary component. In this circumstance, the magnitude of the reflection coefficient varies between 0 and 1, while the phase shift of the reflected wave remains fixed at 0° for $R_0 \geq Z_0$, or 180° for $R_0 < Z_0$.

According to (1), when Z_0 is a real number, the load impedance must be a complex number to generate the quadrature component necessary for IQ modulation. In this scenario, it is impossible to continuously adjust the magnitude of the reflection coefficient by simply altering the resistance of the load impedance. To tackle this issue, in our design, the capacitive network includes three stages, designated as Z_1 to Z_3 in Fig. 5. Connecting different stages of this network to the matching circuit yields a reflection coefficient with a consistent phase of -90° and three selectable amplitudes increasing stepwise from 0.3 to 0.9. Conversely, Z_4 to Z_6 form a three-stage inductive network that produces a reflection coefficient with a consistent phase of 90° , and three optional amplitudes ranging from 0.3 to 0.9.

With the architecture depicted in Fig. 5, the MCU can effectively manipulate both the phase and magnitude of the reflection coefficient by adjusting the resistance of the potentiometer and the ON/OFF status of the NMOS transistors in each stage of the load network. In the following section, we will introduce the selection of Z_0 and discuss the strategy for managing the high dynamic range of the acoustic signal in the circuit design.

B. High-Impedance Matching

In the design of the load network for UA-RIS, we match the reflector's impedance to $1\text{ k}\Omega$ (i.e., $Z_0 = 1\text{ k}\Omega$), a value substantially higher than the standard $50\ \Omega$ or $75\ \Omega$ commonly employed in radio communication systems. This significant divergence is attributed to the inherent resistance introduced by the wiper of the programmable potentiometer.

In an ideal potentiometer, the resistance between a terminal and the wiper should vary continuously from 0 to R_{max} , where R_{max} is the resistance between the two terminals. However, in a real programmable potentiometer, an array of MOSFETs is usually employed to emulate the function of a mechanical wiper for resistance adjustment. These MOSFETs inherently exhibit a certain level of resistance.

In order to precisely control the phase and amplitude of the quadrature component for accurate IQ modulation, the wiper resistance of programmable potentiometers cannot be ignored. For instance, models such as the AD8403 [26] and AD5245 [27] typically exhibit a wiper resistance of about $50\ \Omega$, while the MAX5427 has a resistance of $100\ \Omega$ [28]. Consequently, the minimum resistance of the load network in (1) does not approach zero but remains significantly higher. In scenarios where the impedance of the reflector is matched to $50\ \Omega$ (i.e., $Z_0 = 50\ \Omega$), the reflection coefficient consistently remains positive. As a result, the reflector will be incapable of generating an antiphase wave.

To address the aforementioned problem, we match the impedance of the acoustic reflector to $1\text{ k}\Omega$, significantly higher than the inherent wiper resistance of the programmable potentiometer. This configuration allows the MCU to flexibly adjust the amplitude of the quadrature component between -1 and 1 by programming the resistance of the potentiometer.

C. Highly Dynamic Incident Waves

In practical scenarios, the distance between the UA-RIS and the acoustic transmitter may be unknown or can change over time in mobile applications. As a result, the intensity of the acoustic waves reaching the UA-RIS can vary significantly. To ensure the reliability of the UA-RIS, it is crucial that the hardware performs consistently across environments with both high and low energy densities.

Acoustic signals naturally consist of periodic compressions and rarefactions within the medium. Consequently, the output from a reflector is always alternating current (AC). Therefore, the electronic switches in a UA-RIS must be capable of handling bidirectional current flow. Taking NMOS transistors as an example, when the incident power is weak, a single MOSFET can be utilized as an electronic switch to control the ON and OFF states of the load. However, as the intensity of the incident power increases, the intrinsic body diode of the NMOS transistor conducts during the negative half-cycle of the signal. Under these conditions, the load remains connected for half the signal cycle even if the gate-to-source voltage of the transistor falls below a threshold.

To mitigate the aforementioned issue, we pair MOSFETs as an electronic switch. As depicted in Fig. 5, the source terminal of the upper NMOS transistor is connected to the drain terminal of the lower one. This arrangement allows the body diode of the lower transistor to effectively prevent any reverse current in the load network. However, this setup necessitates at least an additional transistor and a pull-down resistor, denoted by R_{pd} in the figure, for each stage of the load network. Consequently, this escalates the overall cost of the UA-RIS, especially when a large number of acoustic reflectors are incorporated to support long-distance underwater communication.

VI. PERFORMANCE EVALUATION

This section evaluates the performance of the proposed UA-RIS through experiments. Initially, we examine the power consumption of the system. Subsequently, the results collected from both tank and lake environments are presented to demonstrate the viability of the UA-RIS in real-world applications.

A. Power Consumption

Although the UA-RIS does not transmit acoustic signals, it still requires an energy supply to maintain the operation of active components for IQ modulation. In our implementation, the power consumption of the system primarily originates from four components: the MCU, twelve I/O extenders, and six programmable potentiometers. In this section, we thoroughly analyze the power consumption of UA-RIS operating in various states.

In the absence of target waves, the UA-RIS remains in standby mode to save the energy. In this mode, the current consumption for the ATmega256RFR2 MCU, TCA9555 I/O extender with high inputs, and AD8403AR50 potentiometer at a 2 V supply voltage are 650 nA , 500 nA , and $5\ \mu\text{A}$, respectively. Consequently, the total power consumption of the system is only $73.3\ \mu\text{W}$. However, upon detection of acoustic signals, UA-RIS transitions to an active mode. In this scenario, the power consumption of the system is divided into two stages: (a) the impedance adjustment phase, and (b) the impedance maintenance phase.

In the impedance adjustment phase, the MCU controls the I/O extender and AD8403AR50 potentiometer to finely tune the load impedance in alignment with the desired direction of the reflected waves. In the worst case, all load impedances shift from reactance to resistance, necessitating concurrent programming of all potentiometers. To achieve this, the MCU sends three bytes of data (chip address + register address + output value) via the I²C protocol to manage the I/O extender for each channel. Additionally, it transmits two bytes (channel ID and value) through the SPI protocol to set the resistance for each potentiometer. As a result, the MCU issues a total number of 72 bytes and 48 bytes through the I²C and SPI protocols, respectively.

After completing the load configuration, the circuit transitions into the impedance maintenance phase. In this phase, the MCU can enter a sleep mode, while the I/O extender and potentiometer continue to operate, maintaining the states of electronic switches and load impedance during a signal period for beam steering. At this time, the power consumption of the UA-RIS lies between that of the standby mode and the first phase of the active mode.

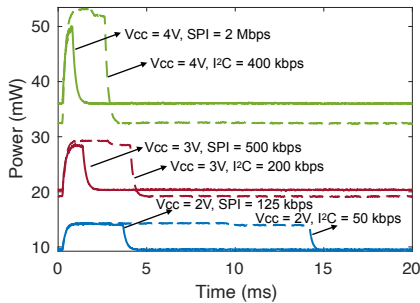


Figure 6: Power consumption of the UA-RIS at various supply voltages.

Fig. 6 displays the power consumption of the UA-RIS in the active mode, in which the MCU updates the outputs of the I/O extender and adjusts the resistance of the potentiometer across all 24 reflectors. For this experiment, the MCU operates at 8 MHz, and the system is powered by a Keysight EDU36311A DC supply. In the figure, the peaks of the waveform corresponding to I²C or SPI communications occur at a specified supply voltage during the impedance adjustment phase, while the subsequent data illustrate the power consumption during the impedance maintenance phase.

As depicted in Fig. 6, the overall system power consumption in active mode varies significantly with changes in the supply voltage, denoted by V_{cc} . For instance, at a V_{cc} of 2 V, the peak power consumed for I²C or SPI serial communication is only 14.2 mW. However, when V_{cc} is increased to 4 V, the power consumption rises to 53 mW, a 3.7-fold increase compared to the lower supply voltage. Similarly, power consumption during the impedance maintenance phase is also proportional to V_{cc} . At 2 V, maintaining the load impedance of 24 channels consumes only 9.3 mW, whereas at 4 V, this consumption escalates to 35.3 mW.

Table I details the energy spent in the two phases of active mode, where the length of the acoustic signal is 1 second. The results demonstrate that higher data rates can substantially reduce transmission time, thus lowering energy consumption in phase 1. For example, at a 2 V supply voltage, with I²C

Table I: Energy/power consumption in the active mode

V_{cc}	Phase I						Phase II (mJ)
	I ² C (μ J)			SPI (μ J)			
	50 (kbps)	200 (kbps)	400 (kbps)	125 (kbps)	500 (kbps)	2 (Mbps)	
2 V	198.5	56.6	38.4	48.9	15.3	8.8	9.3
3 V	397.0	112.4	73.7	98.1	33.6	18.0	19.9
4 V	694.7	198.4	127.7	172.5	58.6	31.8	35.3

and SPI baud rates at 50 kbps and 125 kbps, respectively, the energy consumed for serial communication are 198.5 μ J and 48.9 μ J, respectively, totaling 247.4 μ J for the first phase. In contrast, increasing the baud rate of I²C to 400 kbps, and SPI to 2 Mbps, the maximum speeds supported by the ATmega256RFR2 MCU, reduces the energy consumption in phase 1 to 47.2 μ J (38.4 μ J + 8.8 μ J), which is only one-fifth of the earlier scenario.

Due to the long preambles associated with slow data rates, the duration of underwater acoustic signals is significantly longer than that of RF signals [21]. Consequently, the UA-RIS must maintain the load impedance for hundreds of milliseconds or longer to accommodate a complete signal period, resulting in substantial energy consumption. According to Table I, when the supply voltage is 2 V and serial communication occurs at maximum speed, over 95% of the energy is consumed in phase 2. Increasing the supply voltage to 4 V raises this proportion to 99.6%.

B. Tank Experiments

1) *Experimental settings:* Before evaluating the performance of the entire system in the lake, we first verified the functionality of a single reflection unit in a tank environment. The experimental setup is shown in Fig. 7, where two BTEch Acoustic BT-2RCL [29] omnidirectional acoustic transducers serve as the transmitter and receiver, respectively. The transmitter is driven by a Siglent 1062X arbitrary waveform generator, emitting a 28.23 kHz continuous wave (CW) with a peak-to-peak voltage of 20.0 V. The receiver is connected to a Siglent 1104X-E digital oscilloscope for data acquisition.

Four reflectors are placed at the bottom of the tank, with a spacing of 6.4 cm (1.2 wavelengths at 28.23 kHz) between neighboring reflectors. In the experiments, impedance matching between the transducer and the signal generator or oscilloscope was not performed, as our focus was on the relative changes in the received signal strength influenced by the reflector, rather than the absolute values.

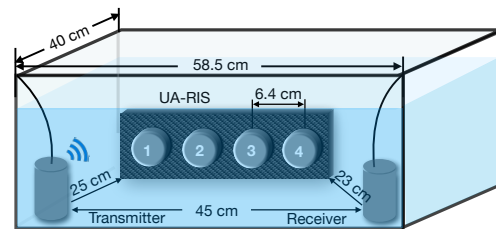


Figure 7: Settings of tank tests.

2) *Resistive load modulation:* In Fig. 8, the MCU is programmed to perform 1-bit coding, periodically switching the

load resistance of a specific reflector between short-circuit and open-circuit with durations of 60 ms and 200 ms, respectively. This configuration generates reflected waves with opposite phases. As depicted in the figure, altering the load resistance of the acoustic reflector remarkably affects the strength of the received signal. Using reflector 2 as an example, the voltage of the received signal is only 9 mV with the short-circuit (0 load impedance). In contrast, when the circuit is open (∞ load impedance), the received signal increases to 65 mV, 7.2 times higher than in the short-circuit condition.

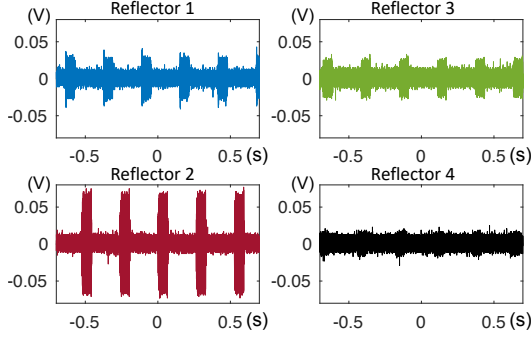


Figure 8: Received signal strength with one selected reflector programmed for 1-bit coding at a time.

Additionally, Fig. 8 demonstrates that changes in the reflector significantly affect the strength of the received signal. This is due to the proximity of the transmitter, receiver, and reflector, creating a near-field environment for acoustic propagation. Furthermore, the small size of the tank and its smooth surface contribute to rich multipath channels of the acoustic waves. With this setup, even slight adjustments to the reflector's position can have a dramatic impact on the received signal strength. For instance, when the load impedance of reflector 1 toggles between 0 and ∞ , the received signal voltage shifts from 29 mV to 13 mV. In contrast, reflector 4 shows a much smaller change, with the voltage varying only between 19 mV and 13 mV, illustrating a less pronounced difference.

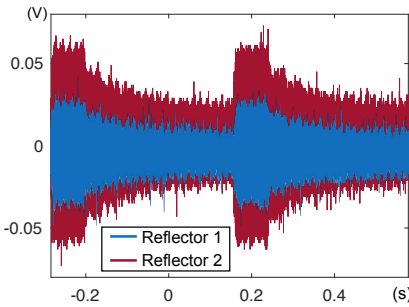


Figure 9: Variation in strength of the received signal with changes in potentiometer's resistance.

In Fig. 9, the resistive network is connected to the reflector, and then the MCU adjusts the potentiometer's resistance to vary from $50\ \Omega$ to $1.96\ \text{k}\Omega$ in $200\ \Omega$ increments. The results in the figure demonstrate that the digital potentiometer can effectively control the amplitude of the reflected wave, enabling precise adjustments to the received signal strength. Using reflector 2 as an example, when the load resistance is set

to $50\ \Omega$, the reflected waves simulate a short-circuit condition, resulting in a relatively high signal strength of 63 mV. As the resistance increases, the reflected wave gradually shifts toward an open-circuit situation, reducing the signal strength to 23 mV. At the maximum resistance of $50\ \text{k}\Omega$, supported by the AD8403AR50 potentiometer, the strength of the received signal can further decrease to approximately 9 mV.

In the tank experiments, the received signals consist of a mixture of three components: (a) the direct wave, (b) waves reflected by the reflector one or more times, and (c) other multipath signals that do not interact with the reflector. The results presented in Fig. 8 and Fig. 9 reflect the combined effects of these three components. An intriguing question arises: how does a UA-RIS contribute to the received signal in an unbounded space? In other words, we aim to isolate component (b) to analyze its specific contribution to enhancing the strength of the received signal.

To achieve the above objective, let $s(t)$ and $r(t)$ represent the source and received signals at time t , respectively. Taking multipath effects into account, when the reflector's load states are in open-circuit and short-circuit, the corresponding received signals, which are denoted by $r_{op}(t)$ and $r_{sh}(t)$, respectively, can be described as follows:

$$\begin{cases} r_{op}(t) = \sum_{i=1}^N A_i e^{j\psi_i} s(t - \tau_i) + \sum_{k=1}^M B_k e^{j\phi_k} s(t - \tau_k), \\ r_{sh}(t) = \sum_{i=1}^N A_i e^{j\psi_i} s(t - \tau_i) + \sum_{k=1}^M B'_k e^{j\phi'_k} s(t - \tau_k), \end{cases} \quad (6)$$

where A_i and ψ_i are the amplitude and phase of the channel coefficient for the direct wave and the multipath signals that do not interact with the reflector. B_k and ϕ_k are the amplitude and phase of the channel coefficient for waves reflected by the reflector with infinite load impedance (open-circuit); B'_k and ϕ'_k are that with zero load impedance (short-circuit).

In the second term of (6), we restrict our consideration to waves reflected only once by the reflector since waves reflected multiple times are greatly attenuated and thus contribute minimally to the outcomes. With this restriction, $B'_k e^{j\phi'_k} = -B_k e^{j\phi_k}$ as the amplitudes of signals reflected by the reflector with 0 and ∞ load impedances are equivalent, though their phases are opposite. Consequently, for $[r_{op}(t) - r_{sh}(t)]/2$, only the waves once reflected by the reflector remain. Conversely, for $[r_{op}(t) + r_{sh}(t)]/2$, only the first term of the equations persists, representing the signal unaffected by the acoustic reflector. Subsequently, we will demonstrate the waveform of these terms through experimental results.

In Fig. 10, the waveform generator emits a burst sinusoidal signal consisting of 1500 cycles. The peak-to-peak voltage and frequency of the source signal are set at 20 V and 28.23 kHz, respectively, identical to those presented in Fig. 8. As illustrated in the figure, due to the multipath effect, the beginnings and ends of r_{op} and r_{sh} exhibit significant fluctuations lasting approximately 15 ms. Once all multipath signals have arrived at the receiver, the combined signal becomes stable.

From Fig. 10, it can be observed that the wave generated by the acoustic reflector, i.e., $[r_{op}(t) - r_{sh}(t)]/2$, is smooth. This indicates that the channel environment is consistent and that signals r_{op} and r_{sh} collected at different times are well aligned, ensuring the validity of subsequent anal-

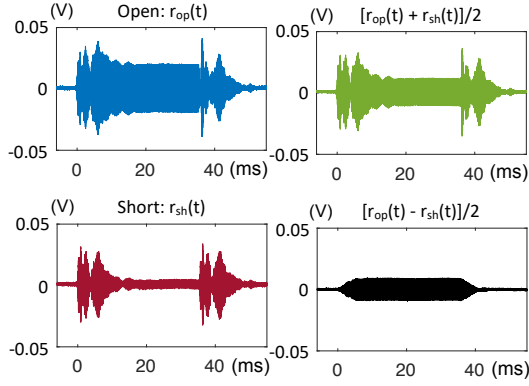


Figure 10: Waveform comparison of received signals with and without the reflector.

ysis. By comparing the waveforms of $[r_{op}(t) + r_{sh}(t)]/2$ and $[r_{op}(t) - r_{sh}(t)]/2$, we have that the amplitude of the received signal created by a single reflector reaches 8.6 mV, which is comparable to that generated by the sum of signals unaffected by the acoustic reflector. This result demonstrates the effectiveness of the constructed acoustic reflector and load network in manipulating the strength of the received signal.

3) *Reactive load modulation*: The multipath model presented in (6) can also be used to validate the reflector's ability to produce the quadrature component for IQ modulation. This can be achieved by programming the MCU to sequentially connect the subnetwork shown in Fig. 5 with the acoustic reflector. The waveform of the received signal is depicted in Fig. 11 (a)¹, where the source is 28.23 kHz CW with 20 V peak-to-peak voltage. In the figure, labels such as C0.3 and L0.9 indicate that the acoustic reflector is connected to the capacitive and inductive load network with reflection coefficients of 0.3 and 0.9 amplitude, respectively.

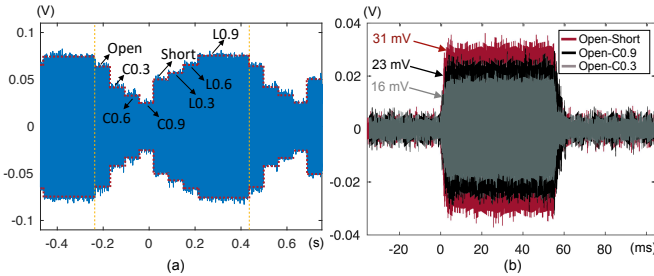


Figure 11: Waveform of the received signal with variations in load impedance. (a) Original waveform. (b) Differential waveforms.

As depicted in Fig. 11 (a), the received signal strength varies markedly when different reactive loads are connected to the reflector. For example, with a capacitive load labeled C0.9, the amplitude of the received signal is only 23 mV. However, when switching to an inductive load labeled L0.9, the amplitude of the received wave increases to 72 mV, which is 3.1 times greater than that observed with the previous capacitive load.

The results in Fig. 11 (a) illustrate only the amplitude of the received signal influenced by the multipath effect. To

¹The experiment in Fig. 11 was conducted on a different day than those in Figs. 8 to 10. This difference resulted in varying acoustic environments and channel states, indicating that this experiment should be considered independent.

accurately evaluate the phase and magnitude of the reflected wave generated by each reactive load, we need to further apply the approach outlined in Fig. 10. In this approach, the waveform generator transmits a burst sinusoidal signal consisting of 1500 cycles at 28.23 kHz with a 20 V peak-to-peak voltage, followed by calculating the strength of the differential signals produced by the reflector with various load impedances.

Let $r_{c.9}$, and $r_{c.3}$ represent the received signals corresponding to the load conditions of the acoustic reflector being at C0.9, and C0.3, respectively. As outlined in Section V-A, the reflection coefficients for the reflector with load impedances r_{op} , r_{sh} , $r_{c.9}$, and $r_{c.3}$ are 1, -1 , $0.9e^{-j\frac{2\pi}{\pi}}$, and $0.3e^{-j\frac{2\pi}{\pi}}$, respectively. Consequently, based on equation (6), we have that

$$\begin{cases} r_{op}(t) - r_{sh}(t) = 2 \sum_{k=1}^M B_k e^{j\phi_k} s(t - \tau_k), \\ r_{op}(t) - r_{c.9}(t) = \left(1 - 0.9 e^{-j\frac{\pi}{2}}\right) \sum_{k=1}^M B_k e^{j\phi_k} s(t - \tau_k), \\ r_{op}(t) - r_{c.3}(t) = \left(1 - 0.3 e^{-j\frac{\pi}{2}}\right) \sum_{k=1}^M B_k e^{j\phi_k} s(t - \tau_k). \end{cases} \quad (7)$$

According to (7), the following ratio can be obtained:

$$\begin{aligned} |r_{op}(t) - r_{sh}(t)| : |r_{op}(t) - r_{c.9}(t)| : |r_{op}(t) - r_{c.3}(t)| \\ = 2 : \left|1 - 0.9 e^{-j\frac{\pi}{2}}\right| : \left|1 - 0.3 e^{-j\frac{\pi}{2}}\right| \\ = 1 : 0.68 : 0.52. \end{aligned} \quad (8)$$

Now, we can use the above ratio to check the accuracy of the quadrature component generated by the reflector. As shown in Fig. 11 (b), the average strengths of differential signals $r_{op} - r_{sh}$, $r_{op} - r_{c.9}$, and $r_{op} - r_{c.3}$ are 31 mV, 23 mV, and 16 mV, respectively; the ratio of these values is 1: 0.74: 0.52, close to the idea case calculated in (8). This validates the ability of the constructed reflector to generate the negative quadrature component for IQ modulation.

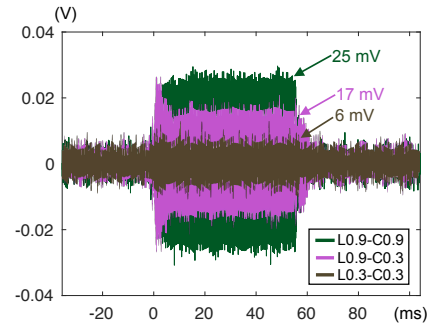


Figure 12: Differential signal with inductive and capacitive loads at the acoustic reflector.

We also checked the differential waves with inductive load

at the reflector using the following ratio:

$$\begin{aligned} & |r_{l,9}(t) - r_{c,9}(t)| : |r_{l,9}(t) - r_{c,3}(t)| : |r_{l,3}(t) - r_{c,3}(t)| \\ &= 0.9 \times \left| e^{\frac{j\pi}{2}} - e^{-\frac{j\pi}{2}} \right| : 0.3 \times \left| 0.3 e^{\frac{j\pi}{2}} - e^{-\frac{j\pi}{2}} \right| : 0.3 \times \left| e^{\frac{j\pi}{2}} - e^{-\frac{j\pi}{2}} \right| \\ &= 1 : 0.67 : 0.33, \end{aligned} \quad (9)$$

where $r_{l,9}$ and $r_{l,3}$ represent the received signals corresponding to the load conditions of the acoustic reflector being in L0.9 and L0.3, respectively.

As illustrated in Fig. 12, the average strengths of differential signals $r_{l,9} - r_{c,9}$, $r_{l,9} - r_{c,3}$, and $r_{l,3} - r_{c,3}$ are 25 mV, 17 mV, and 6 mV, respectively; the ratio of these values is 1 : 0.68 : 0.24, close to the idea case calculated in (9). This result validates the ability of the constructed reflector to generate the positive quadrature component for IQ modulation.

C. Lake Tests

1) *Experimental setup*: We conducted lake experiments to validate the functionality of our UA-RIS system. The control board and the reflecting array are depicted in Fig. 13(a) and Fig. 13(b), respectively, while the experimental setup is illustrated in Fig. 13(c).

In the test, the arbitrary waveform generator emitted a 28 kHz CW signal at 15 dBm. This signal was then amplified using a Fosi M03 audio power amplifier to drive the BTech omnidirectional acoustic transducer. At the receiving end, another BTech transducer positioned 21 m away from the transmitter captured the acoustic signal. The received waveform was initially amplified by a Sound Devices MM-1 microphone amplifier, which provided a 54 dB gain, and then recorded with a PicoScope 4224 portable oscilloscope.

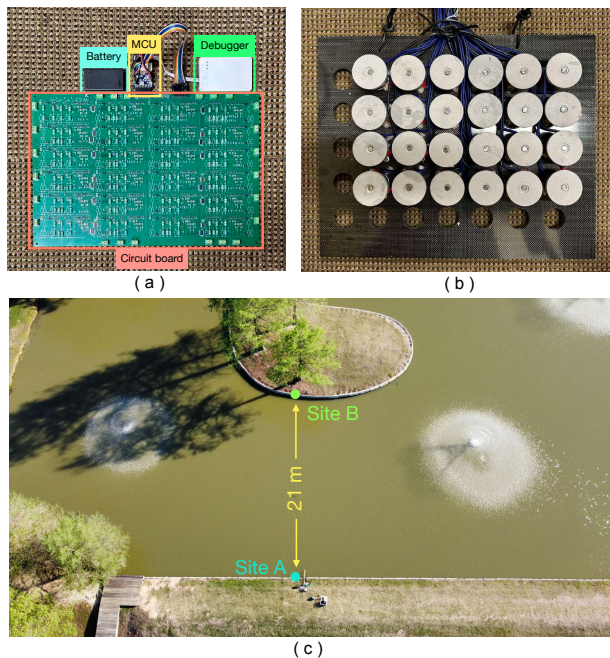


Figure 13: Lake experiments. (a) 24-channel control board. (b) Acoustic reflection units. (c) Experimental setup.

2) *UA-RIS close to sender*: As shown in Fig. 13(c), in the initial lake test, the receiver was deployed at site B, while the transmitter and the UA-RIS were located at site A, with the

latter positioned 15 wavelengths behind the former. From the receiver's perspective, this setup emulates a scenario where an acoustic signal from a virtual source travels a certain distance before being reflected by a UA-RIS positioned 21 meters away. By adjusting the emission power of the signal generator or the gain of the power amplifier, we can replicate different distances of signal propagation between the virtual source and the UA-RIS.

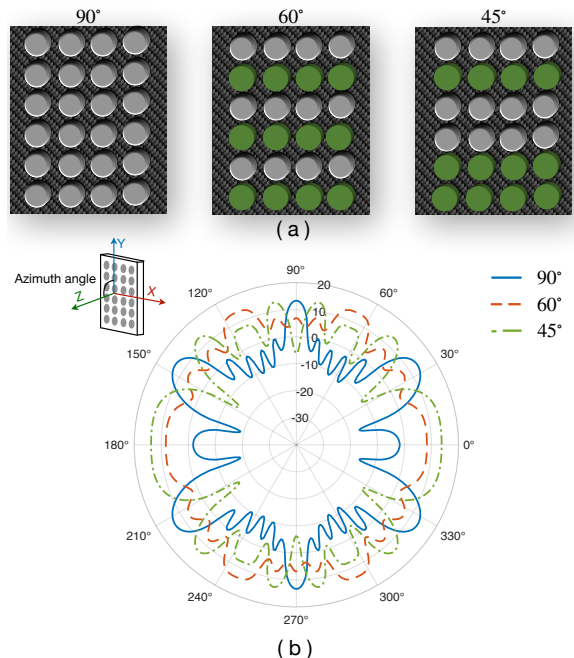


Figure 14: Load configuration of UA-RIS for beamforming at the transmitter side. (a) Coding schemes for steering. (b) Azimuth beam pattern of the reflected waves.

The diagrams of the three load configurations, i.e., the coding schemes used in the first test, are depicted in Fig. 14(a). In these diagrams, the initial loads of the gray and green reflectors are set to open and short-circuits, respectively. The coordinate system and the azimuth beam patterns generated by these three coding schemes are illustrated in Fig. 14(b).

In Figure 15, the UA-RIS toggles the load of each reflector between short-circuit and open-circuit states every 20 ms, following the initial load coding scheme illustrated in Fig. 14(a). This configuration results in varying levels of received signal strength, influenced by the beam pattern generated by UA-RIS. Notably, when the azimuth angle of the main beam is set to 90°, the reflected waves align directly with the receiver's direction. This alignment leads to amplitude variations averaging 280 mV and peaking at up to 400 mV as the reflector's load cycles between the two states. In contrast, when the beam's azimuth angles are adjusted to 60° and 45°, the differential voltage at the receiver decreases markedly to 100 mV and 33 mV, respectively. This reduction is due to the main lobe of the reflected waves deviating from the receiver's direct path, which diminishes wave superposition at the receiver. Consequently, this lessens the impact of the reflected wave on the received signal strength.

Based on Fig. 15, we can deduce the potential enhancement in data rate achievable with the UA-RIS. As depicted in the figure, directing the main beam to 90° elevates the received signal from 1 V (blue line at 320 ms) to an average of 1.28 V,

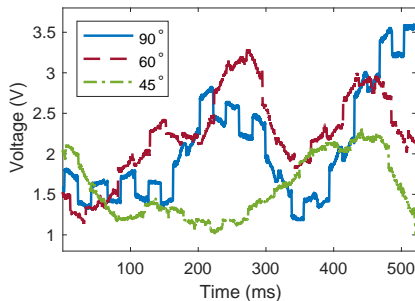


Figure 15: Envelopes of received signals with various coding schemes implemented at UA-RIS.

yielding a 2.15 dB increase in SNR. Under these conditions, employing frequency-shift keying (FSK) or phase-shift keying (PSK) modulations could increase the data rate by approximately 63.8% while maintaining the same BER. In the optimal scenario, with a 400 mV increase in the received signal, the SNR improvement reaches 2.9 dB, potentially boosting the data rate by up to 96% compared to configurations without UA-RIS.

Now, let's assess the impact of UA-RIS on communication range. Suppose the initial communication distance to be 0.5 km. If the received voltage increases from 1 V to 1.4 V, this corresponds to a gain of 3 dB in signal pressure at the receiver side. Given these parameters, we can derive the following equation:

$$10\alpha(\log_{10} R_y - \log_{10} R_x) + \beta(R_y - R_x) = \Delta\text{SNR}, \quad (10)$$

where $R_x = 0.5$ km represents the original communication distance. R_y denotes the extended communication range achieved with the support of UA-RIS. $\Delta\text{SNR} = 2.9$ dB is the received SNR gain achieved by the UA-RIS. The spreading coefficient, denoted by α , is 1 for cylindrical waves and 2 for spherical waves. The coefficient β represents the absorption loss of acoustic waves. According to the Francois-Garrison model [30], $\beta = 6.1$ dB/km for a 28 kHz acoustic signal in seawater under typical conditions (10°C temperature, 35 ppt salinity, and pH 8).

Referring to (10), we have that in deep water environments, where $\alpha = 2$ for spherical spreading, R_y can reach 0.64 km. With the support of UA-RIS, the communication range is extended by 28%. In shallow water environments, characterized by $\alpha = 1$ for cylindrical spreading, R_y further extends to 0.73 km, marking a 46% enhancement from the original range.

3) *UA-RIS close to receiver*: In the second lake test, the transmitter and receiver remained in their original positions, while the UA-RIS was moved to site B, 15 wavelengths behind the receiver. To evaluate the UA-RIS's performance with IQ modulation, three different load coding schemes were applied. As illustrated in Fig. 16 (a), the initial load settings for the gray, green, purple, and orange reflectors were configured to open, short, L1.0, and C1.0, respectively. The azimuth beam patterns resulting from these coding schemes are shown in Fig. 16 (b), where the main lobes of the reflected beams are directed at 90°, 73°, and 180°, respectively.

In Fig. 17, the UA-RIS alternates the load of each reflector between short-circuit and open-circuit or L10 and C10 every 66 ms, following the initial coding scheme depicted in Fig. 16 (a). From the figure, significant variations in the

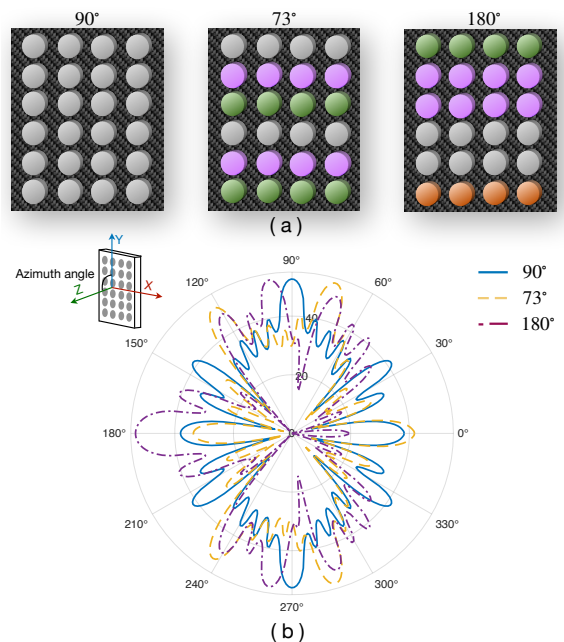


Figure 16: Load configuration of UA-RIS for beamforming at the receiver side. (a) Coding schemes for steering. (b) Azimuth beam pattern of the reflected waves.

intensity of the received signal can be observed, which are dependent on the beam pattern generated by the UA-RIS.

When the main lobe of the reflected beam is directed at 90° towards the receiver, the strength of the received signal is considerably enhanced. Specifically, as the reflector's load cycles between the two states, the average amplitude variation is 1.04 V, with the maximum variation reaching up to 1.4 V. In contrast, when the beam is steered to 73° and 180°, the main lobe of the reflected wave deviates from the receiver's direction, resulting in reduced average amplitude variations of 0.51 V and 0.08 V, respectively.

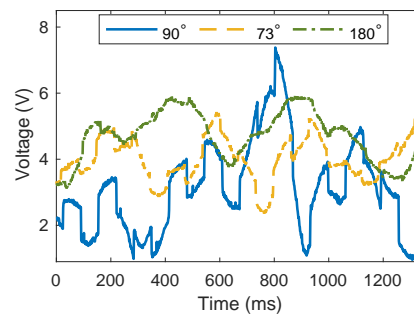


Figure 17: Envelopes of received signals with various coding schemes implemented at UA-RIS.

Referring to Fig. 17, the implementation of the UA-RIS on the receiver side can significantly enhance both the data rate or the communication range. When the beam of the reflected wave targets the receiver, the UA-RIS elevates the voltage of the received signal from 1.75 V to 2.83 V (as indicated by the blue line at 150 ms), yielding a maximum SNR gain of approximately 4.2 dB. This enhancement allows for a potential increase in the data rate by 163% for both FSK and BPSK modulation schemes, while maintaining the same BER. On

average, the UA-RIS boosts the received signal voltage from 3.04 V to 4.08 V, resulting in an SNR gain of 2.56 dB, and facilitating an average of 80.3% data rate increment.

Considering an initial communication distance of 0.5 km between the transceiver units, and applying (10), the communication distance in a deep-water environment can be extended to 0.7 km with the 4.2 dB SNR gain, translating to an approximate 40.6% increase in range while preserving the same BER. In shallow water scenarios, characterized by a spreading coefficient of 1, the communication distance can be further extended to 0.83 km, thus augmenting the communication range by about 66%.

VII. CONCLUSION AND FUTURE WORK

In this paper, we explored the design of UA-RIS to enhance the range and speed of underwater acoustic communications. We addressed several challenging issues critical to system implementation, including wide dynamic range and low frequency of acoustic signals. To optimize performance, the proposed UA-RIS strategically aligns reflection units based on the angles of incident waves and their intended directions, utilizing IQ modulation to shape the reflected waves. This approach can precise control over the phase and amplitude of the signals, enabling advanced beam-steering capabilities.

Results from tank experiments demonstrated the capability of acoustic reflectors to finely tune the phase and amplitude of signals by adjusting the load impedance. Additionally, we evaluated a UA-RIS setup comprising 24 reflection units during lake trials, which proved effective in significantly enhancing or diminishing signal strength in designated directions. This adjustment improved receiving SNR and minimized interference at specific locations. Experimental results suggest that, by deploying the UA-RIS close to the sender, the communication range in deep and shallow water environments can be extended by 28% and 46%, respectively. When the distance between communicating parties remains constant, data transmission rates employing modulation schemes like FSK or PSK can be increased by an average of 63.8%, and in some cases, up to 96% with the support of UA-RIS. In addition, moving the UA-RIS near the receiver extends the communication range in both deep and shallow water environments by 40.6% and 66%, respectively. Furthermore, with the distance fixed, situating the UA-RIS near the receiver not only improves data rates by an average of 80.3% but can also achieve increases of up to 163% under specific conditions.

UA-RIS technology is still in its early stages, its real-world deployment requires further development. In particular, integrating this new technology into existing systems necessitates critical modifications to current medium access control protocols. Adapting these protocols will enable the seamless integration of UA-RIS into established underwater network infrastructures, a topic we intend to investigate in our future research.

REFERENCES

- [1] H. Yang, S. Kim, H. Kim, S. Bang, Y. Kim, S. Kim, K. Park, D. Kwon, and J. Oh, "Beyond limitations of 5g with ris: Field trial in a commercial network, recent advances, and future directions," *IEEE Communications Magazine*, 2023.
- [2] Q. Wu, B. Zheng, C. You, L. Zhu, K. Shen, X. Shao, W. Mei, B. Di, H. Zhang, E. Basar *et al.*, "Intelligent surfaces empowered wireless network: Recent advances and the road to 6g," *Proceedings of the IEEE*, 2024.
- [3] Z. Sun, H. Guo, and I. F. Akyildiz, "High-data-rate long-range underwater communications via acoustic reconfigurable intelligent surfaces," *IEEE Communications Magazine*, vol. 60, no. 10, pp. 96–102, 2022.
- [4] H. Wang, Z. Sun, H. Guo, P. Wang, and I. F. Akyildiz, "Designing acoustic reconfigurable intelligent surface for underwater communications," *IEEE Transactions on Wireless Communications*, 2023.
- [5] T. Kelly, *Prototyping a Power Take-off for the Wirewalker Wave-powered Profiling Vehicle*. University of California, San Diego, 2023.
- [6] J. Kim, J. Kim, J. H. Oh, S.-H. Wi, and J. Oh, "Rotated feed-combined reconfigurable transmit RIS with disparate deployment of 1-bit hybrid units for B5G/6G," *IEEE Transactions on Antennas and Propagation*, vol. 71, no. 6, pp. 5457–5462, 2023.
- [7] H. L. Van Trees, *Optimum array processing: part IV of detection, estimation, and modulation theory*. John Wiley & Sons, 2002.
- [8] B. A. Munk, *Frequency selective surfaces: theory and design*. John Wiley & Sons, 2005.
- [9] N. Engheta and R. W. Ziolkowski, *Metamaterials: physics and engineering explorations*. John Wiley & Sons, 2006.
- [10] T. J. Cui, M. Q. Qi, X. Wan, J. Zhao, and Q. Cheng, "Coding metamaterials, digital metamaterials and programmable metamaterials," *Light: science & applications*, vol. 3, no. 10, pp. e218–e218, 2014.
- [11] S. Hassouna, M. A. Jamsheh, J. Rains, J. u. R. Kazim, M. U. Rehman, M. Abualhayja, L. Mohjazi, T. J. Cui, M. A. Imran, and Q. H. Abbasi, "A survey on reconfigurable intelligent surfaces: wireless communication perspective," *IET Communications*, vol. 17, no. 5, pp. 497–537, 2023.
- [12] F. Naeem, M. Ali, G. Kaddoum, C. Huang, and C. Yuen, "Security and privacy for reconfigurable intelligent surface in 6G: a review of prospective applications and challenges," *IEEE Open Journal of the Communications Society*, 2023.
- [13] L. Boccia, F. Venneri, G. Amendola, and G. Di Massa, "Application of varactor diodes for reflectarray phase control," in *IEEE Antennas and Propagation Society International Symposium*, vol. 3. IEEE, 2002, p. 132.
- [14] S. V. Hum, M. Okoniewski, and R. J. Davies, "Modeling and design of electronically tunable reflectarrays," *IEEE transactions on Antennas and Propagation*, vol. 55, no. 8, pp. 2200–2210, 2007.
- [15] X. Tan, Z. Sun, J. M. Jornet, and D. Pados, "Increasing indoor spectrum sharing capacity using smart reflect-array," in *2016 IEEE International Conference on Communications (ICC)*. IEEE, 2016, pp. 1–6.
- [16] X. Pei, H. Yin, L. Tan, L. Cao, Z. Li, K. Wang, K. Zhang, and E. Björnson, "Ris-aided wireless communications: prototyping, adaptive beamforming, and indoor/outdoor field trials," *IEEE Transactions on Communications*, vol. 69, no. 12, pp. 8627–8640, 2021.
- [17] S. Abeywickrama, R. Zhang, Q. Wu, and C. Yuen, "Intelligent reflecting surface: practical phase shift model and beamforming optimization," *IEEE Transactions on Communications*, vol. 68, no. 9, pp. 5849–5863, 2020.
- [18] B. O. Zhu, J. Zhao, and Y. Feng, "Active impedance metasurface with full 360 reflection phase tuning," *Scientific reports*, vol. 3, no. 1, p. 3059, 2013.
- [19] G. Yu, Y. Qiu, Y. Li, X. Wang, and N. Wang, "Underwater acoustic stealth by a broadband 2-bit coding metasurface," *Physical Review Applied*, vol. 15, no. 6, p. 064064, 2021.
- [20] A. Eid, J. Rademacher, W. Akbar, P. Wang, A. Allam, and F. Adib, "Enabling long-range underwater backscatter via Van Atta acoustic networks," in *Proceedings of the ACM SIGCOMM 2023 Conference*, 2023, pp. 1–19.
- [21] Y. Luo, L. Pu, M. Zuba, Z. Peng, and J.-H. Cui, "Challenges and opportunities of underwater cognitive acoustic networks," *IEEE Transactions on Emerging Topics in Computing*, vol. 2, no. 2, pp. 198–211, 2014.
- [22] W. J. Richardson, C. R. Greene Jr, C. I. Malme, and D. H. Thomson, *Marine mammals and noise*. Academic press, 2013.
- [23] D. M. Oceanographic, "Wirewalker wave-powered profiler," Del Mar Oceanographic LLC, 2021, [Accessed: January, 2024]. [Online]. Available: <https://www.delmarocean.com>
- [24] ZETEX Semiconductors, *830 series silicon 25V hyperabrupt varactor diodes*, ZETEX Semiconductors, Zetex Technology Park, Chadderton Oldham, UK, January 2007.
- [25] NTE Electronics Inc., *NTE618 varactor silicon tuning diode for AM radio*, NTE Electronics Inc., Bloomfield, NJ, USA, March 2012.
- [26] Analog Devices, *1-/2-/4-channel digital Potentiometers AD8400/AD8402/AD8403*, Analog Devices Company, Wilmington, MA, USA, 2010.
- [27] —, *256-Position I2C-compatible digital potentiometer*, Analog Devices Company, Wilmington, MA, USA, April 2022.
- [28] Maxim Integrated, *One-time programmable, linear-taper digital potentiometers*, Maxim Integrated Company, San Jose, CA, USA, 2005.
- [29] B. Acoustics, "BT-2RCL acoustic transducer," BTech Acoustics LLC, 2024, [Accessed: September, 2024]. [Online]. Available: <https://www.btechacoustics.com/products/bt-2rcl>
- [30] X. Lurton, *An introduction to underwater acoustics: principles and applications*. Springer Science & Business Media, 2002.